Aerodynamic Model Identification of a Quadrotor Subjected to Rotor Failures in the High-Speed Flight Regime

Sihao Sun and Coen de Visser

***Abstract*—This letter presents a high-fidelity aerodynamic model of a quadrotor in the high-speed flight, with the normal configuration, or subjected to rotor failures. A novel experimental setup, data processing, and model identification procedure are developed. The main idea is that by first establishing the thrust and torque model from static wind tunnel tests as the benchmark of the aerodynamic model, and then identifying the in-plane forces, pitch and roll moments of each rotor from the free flight data obtained in a large-scale open-jet wind tunnel. The validation results show a decent model performance in predicting forces/moments, lateral forces effects, and the quadrotor trimming curve, by comparing with the benchmark model.**

***Index Terms*—Robot safety, aerial systems: mechanics and control.**

I. Introduction

SINCE the advent of multi-rotor drones, the operating regimes have been extended from hovering to the high-speed conditions (e.g. delivery, drone racing, etc). This motivates researchers to establish reliable aerodynamic models of multi-rotor drones for various purposes, such as rejecting the wind disturbances [1], trajectory refinement [2], design optimization [3], etc.

There is an extensive body of literature discussing the aerodynamic effects on drones. The thrust variation [4]–[6] and blade flapping effects [7], [8] are mostly considered. They can to some extent precisely depict the major forces deviations in the fast flight comparing to the hovering condition. On the other hand, the aerodynamic moments of a single rotor have been discussed in, e.g. Ref. [9]. The difference between the advancing and retreating blade, and the blade flapping are found to be important in contributing to the moments [6]. The observation that the rear rotors require much higher rotational speed than front rotors during the trim condition demonstrates the existence of these aerodynamic moments [10], [11].

Due to limited knowledge of aerodynamic parameters, such as the Renold number of a small-sized rotor, the aforementioned effects are difficult to be modeled from merely physical insights. A more practical approach is using real data to identify the aerodynamic models. Thrust and drag models are mostly seen being identified for control synthesis (see, e.g., [12]–[14]). In comparison, aerodynamic moment models are more complex and identified in only a few pieces of research [11], [15], though these moments are found to be non-trivial especially in the high-speed regime. The model structures adopted in these methods, however, might not be effective for a drone with rotor failures.

In [16], we conducted flights of a quadrotor with complete loss of a rotor in the high-speed condition. Due to the fast spinning on the yaw direction, effects such as the lateral aerodynamic forces were observed. This motivates us to establish an aerodynamic model that could predict these effect and, at the same time, remain effective to quadrotors without failures.

Therefore, in this letter, the high-speed flight data of a quadrotor with single-rotor-failure (SRF), diagonal double-rotor-failure (DRF) and no-failure (NF) are used for aerodynamic model identification, in combination with the wind tunnel static test of a single rotor. In this process, the following problems are resolved:

1) Establish a multi-body aerodynamic model by distinguishing between the rotor system and the airframe generated forces/moments, using only measurements from the inertial measurement unit (IMU) and the motion capturing system.
2) Precisely measure the forces on the center of gravity (c.g.) in the SRF / DRF configuration with the presence of centrifugal force due to the large yaw rate, and the displacement between c.g. and the IMU location.
3) Reconstruction of the local air velocities of the rotors considering attitude estimation errors and reference frame displacements.
4) Select a model structure which ensures both accuracy and simplicity.

As the main contribution, a parametric model of a quadrotor 3-axis force/moment is consequently established which is generally applicable to either low/high-speed flight conditions and to either configuration with/without rotor failures. In addition, the effects such as the lateral forces in SRF and DRF configurations are also captured by the proposed model during the validation procedure. As a consequence, this model can be used in a wide variety of applications such as improving the controller performance while confronting significant wind flow or complete actuator failures.

This letter is organized as follows. Section II introduces the central equations and methodologies of the identification procedure. Section III details the experimental setups. The

Manuscript received February 22, 2019; accepted July 1, 2019. Date of publication July 15, 2019; date of current version August 1, 2019. This letter was recommended for publication by Associate Editor S. Weiss and Editor P. Rocco upon evaluation of the reviewers' comments. *(Corresponding author: Sihao Sun.)*

The authors are with the Faculty of Aerospace Engineering, Delft University of Technology, 2629 HS Delft, The Netherlands (e-mail: s.sun-4@tudelft.nl; c.c.devisser@tudelft.nl).

Digital Object Identifier 10.1109/LRA.2019.2928758

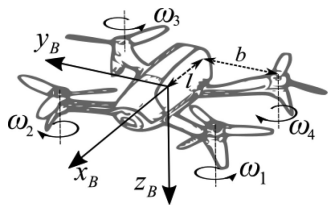

Fig. 1. The tested quadrotor (Parrot Bebop2), the definition of the body frame, the rotor indices and the definition of l and b.

data processing is discussed by Section IV. The selection of model structures and the identification method is described in Section V. In Section VI, the proposed model is validated in both rotor failure and non-failure cases.

II. Methodology

The coordinate systems are first of all introduced. The inertial frame $\{O_I, x_I, y_I, z_I\}$ is originated at a fixed point on the ground. For wind tunnel tests, we define x_I as pointing against the wind flow, y_I pointing right side perpendicular to the wind flow, and z_I aligning with the gravity. The body frame $\{O_B, x_B, y_B, z_B\}$ is originated at the center of gravity with x_B pointing forwards, y_B pointing rightwards, and z_B aligning with the thrust vector but pointing downwards. In the following context, the superscript I and B indicate the coordinate system on which a vector is projected; the subscript i indicates the variable of the ith rotor; the subscript x, y, and z indicate the projection of a vector on the corresponding axis.

The drone used for identification is a modified Parrot Bebop2 as is shown in Fig. 1, where the geometric parameters b and l, and the rotor index definition, are also presented.

Recall the translational and rotational dynamic equations of a quadrotor as

$$\dot{\boldsymbol{V}}^B + \boldsymbol{\Omega}^B \times \boldsymbol{V}^B = \boldsymbol{L}_{BI}\left(\boldsymbol{g}^I - \dot{\boldsymbol{V}}_w^I\right) + \boldsymbol{F}^B/m \tag{1}$$

$$\boldsymbol{I}_v^B\dot{\boldsymbol{\Omega}}^B + \boldsymbol{\Omega}^B \times \boldsymbol{I}_v^B\boldsymbol{\Omega}^B + \left(\boldsymbol{\Omega}^B \times \sum \boldsymbol{I}_p^B\boldsymbol{\omega}_i^B + \sum \boldsymbol{I}_p^B\dot{\boldsymbol{\omega}}_i^B\right) = \boldsymbol{M}^B \tag{2}$$

where $\boldsymbol{V}^B = [u,\ v,\ w]^T$ is the translational velocity of the center of gravity (c.g.) with respect to the airflow, as is projected on the body frame. $\boldsymbol{V}_w^I$ is the wind velocity with respect to the inertial frame. $\boldsymbol{\Omega}^B = [p,\ q,\ r]^T$ is the vehicle's angular velocity with respect to the inertial frame, which is projected in the body frame. The symbol m, $\boldsymbol{I}_v$ and $\boldsymbol{I}_p$ respectively indicate the total mass, moment of inertia of the entire vehicle and of the rotor. $\boldsymbol{L}_{BI}$ is the rotational matrix from the inertial frame to the body frame. $\boldsymbol{\omega}_i^B$ is the angular rate vector of the ith rotor with respect to the inertial frame which is expressed as $\boldsymbol{\omega}_i^B = \boldsymbol{\Omega}^B + [0,\ 0,\ s_{n,i}\omega_i]^T$, where ω_i is the angular rate of the ith rotor with respect to the body frame. $s_{n,i}$ indicates the rotational direction of the ith rotor such that 1 indicates clockwise rotation; for Parrot Bebop2, we have

$$s_n = [-1,\ 1,\ -1,\ 1] \tag{3}$$

The external forces and moments projection on the body frame, denoted by $\boldsymbol{F}^B$ and $\boldsymbol{M}^B$, are composed of control forces/moments and other aerodynamic effects on both rotor systems and the airframe, which is to be determined in this letter. They can be expressed as follows

$$\begin{bmatrix}\boldsymbol{F}^B\\ \boldsymbol{M}^B\end{bmatrix} = \begin{bmatrix}F_x\\ F_y\\ F_z\\ M_x\\ M_y\\ M_z\end{bmatrix} = \begin{bmatrix}\sum F_{x,i}\\ \sum F_{y,i}\\ -\sum T_i\\ \sum s_{l,i}bT_i + \sum M_{x,i}\\ \sum s_{m,i}lT_i + \sum M_{y,i}\\ \sum s_{l,i}bF_{x,i} + \sum s_{m,i}lF_{y,i} + \sum M_{z,i}\end{bmatrix} + \begin{bmatrix}\boldsymbol{F}_f^B\\ \boldsymbol{M}_f^B\end{bmatrix} \tag{4}$$

where $\boldsymbol{F}_f^B$ and $\boldsymbol{M}_f^B$ indicate the 3-axis forces and moments generated by the airframe. $\boldsymbol{F}_i^B = [F_{x,i},\ F_{y,i},\ F_{z,i}]^T$ and $\boldsymbol{M}_i^B = [M_{x,i},\ M_{y,i},\ M_{z,i}]^T$ stand for the 3-axis forces and moments from the ith rotor. By convention, the z_B directions force of each rotor $F_{z,i}$ is replaced by the thrust T_i. Vectors s_l and s_m indicate the direction that each rotor contributes to rolling and pitching; they are

$$s_l = [1,\ -1,\ -1,\ 1], \quad s_m = [1,\ 1,\ -1,\ -1] \tag{5}$$

In this research, the thrust T_i and the z_B direction moment of each rotor $M_{z,i}$ (rotor drag torque by convention) are directly measured during the static test conducted in the wind tunnel, using an off-the-shelf rotor test stand. With T_i and $M_{z,i}$ independently measured instead of identified from the flight data, the aerodynamics on the air-frame can be more accurately estimated (see [11] otherwise). The remaining part of the model, namely the in-plane forces $F_{x,i}$, $F_{y,i}$, the pitch/roll moments $M_{y,i}$, $M_{x,i}$ of each rotor, and the forces/moments from the airframe are identified using the flight data. They are functions of ω_i and the local air velocity of the ith rotor denoted by $\boldsymbol{V}_i^B = [u_i,\ v_i,\ w_i]^T$.

The thrust of the rotor i is expressed as

$$T_i = C_{t,i}\rho(\pi R^2)(\omega_i R)^2 \tag{6}$$

and the drag torque of the rotor i is expressed as

$$M_{z,i} = s_{n,i}C_{q,i}\rho(\pi R^3)(\omega_i R)^2 \tag{7}$$

where ρ is the air density and R is the radius of the rotor. The model of thrust and torque of each rotor will be given in the dimensionless form (C_t and C_q) to increase the generality of this model to drones with different sizes. Define the symbol $|\cdot|$ as the L^2 norm of a vector. Then the $C_{t,i}$ and $C_{q,i}$ can be further characterized as functions of advance ratio J and the angle of attack α, which are defined as

$$J_i = \frac{|\boldsymbol{V}_i|}{\omega_i R}, \quad \alpha_i = \sin^{-1}(w_i/|\boldsymbol{V}_i|) \tag{8}$$

III. Experimental Setup

A. Static Wind Tunnel Test

The static wind tunnel test of a single rotor has been carried out using an off-the-shelf rotor test stand (RCbenchmark series 1580), as Fig. 2 shows. The thrust and the drag torque of a Bebop2 rotor have been measured at the frequency of 4 Hz.

During the static wind tunnel test, the angle of attack α varies from -90 to 90 degrees with steps of 15 degrees. The wind speed

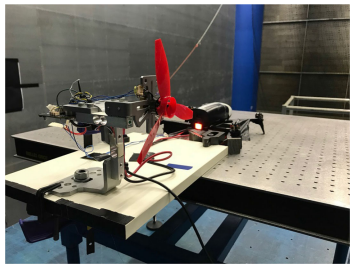

Fig. 2. Setup of the static wind tunnel test of a Bebop2 rotor.

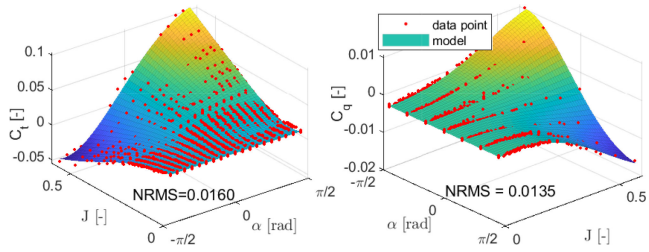

Fig. 3. Model of C_t and C_q in different angles of attack and advance ratios, together with the normalized root mean square (NRMS) of the model residuals.

changes from 0 to 14 m/s in steps of 2 m/s. At each test point, the reference revolutions per minute (RPM) starts from 3000 to 12000 in steps of 1000 RPM. In negative angles of attack, the rotor is mounted such that the thrust pulls the test bench and generate a negative force measurement; on the contrary, the rotor is reversed and push the test bench in the positive angles of attack setups.

The model of C_t and C_q can then be established from (6) and (7). A 5th order polynomial model is used to fit the data as is shown in Fig. 3. The parameters $\boldsymbol{K}_{Ct}$ and $\boldsymbol{K}_{Cq}$ are given in the Appendix. Note that the unit of α is radian.

$$C_t = \mathbf{Q}\boldsymbol{K}_{Ct}, \quad C_q = \mathbf{Q}\boldsymbol{K}_{Cq} \tag{9}$$

$$\mathbf{Q} = [1,\ J,\ J^2,\ J^3,\ J^4,\ J^5,\ J\alpha,\ J^2\alpha,\ J^3\alpha,\ J^4\alpha,\ J\alpha^2,\ J^2\alpha^2,\ J^3\alpha^2,\ J\alpha^3,\ J^2\alpha^3,\ J\alpha^4]$$

B. Flight Test

Since the test bench is only able to measure the thrust and drag torque of rotors, the flight data can be then utilized to identify the rest forces/moments of the rotor and the aerodynamics of the airframe. The flight test has been carried out in the Open Jet Facility (OJF), a large-scale wind tunnel with the aperture of 2.85 m. There is a set of motion capturing system (OptiTrack) including 12 cameras providing the position measurement of the four markers attached to the drone in 120 Hz, with the RMS error less than 0.2 mm. The measurement is transmitted to the on-board autopilot to provide necessary indoor position and velocity information of the drone.

The rest of the measurements are obtained using the on-board sensors at 512 Hz. The implemented IMU is a built-in MPU-6050 MEMS which provides the angular velocity and specific force measurements. The noise performance is 0.005 $\deg \cdot \mathrm{s}^{-1}/\sqrt{\mathrm{Hz}}$ for the gyroscope and 400 $\mu\mathrm{g}/\sqrt{\mathrm{Hz}}$ for the accelerometer. More details can be found in [17]. The IMU ground calibration is conducted to take into account the bias from angular displacements from the IMU to the body frame [18]. An Extended Kalman Filter (EKF) is applied to fuse the OptiTrack and the IMU measurements to obtain the attitude estimation of the body frame. A built-in Brushless DC (BLDC) motor controller on the Parrot Bebop2 measures the rotational speed of each rotor in RPM. The on-board sensor measurements are re-sampled to 120 Hz to synchronize with the OptiTrack measurements.

TABLE I
INERTIAL AND GEOMETRIC PROPERTIES OF THE TESTED QUADROTOR

parameter	value	unit
m_{NF}	0.510	kg
$m_{\mathrm{DRF/SRF}}$	0.410	kg
$\boldsymbol{I}^B_{v,\mathrm{NF}}$	diag(1.92, 1.85, 3.34)×10^{-3}	kgm^2
$\boldsymbol{I}^B_{v,\mathrm{DRF/SRF}}$	diag(1.45, 1.26, 2.52)×10^{-3}	kgm^2
$\boldsymbol{I}^B_p$	diag(4.2, 4.2, 8.0)×10^{-6}	kgm^2
b, l, R	0.115, 0.088, 0.075	m

The flights in three types of configurations are carried out. The no-failure (NF) configuration has been tested in various flight speeds from 0 to 16 m/s, with heading angle towards the nozzle. Next, one or two rotors are removed from the drone to test the single-rotor-failure (SRF) and double-rotor-failure (DRF) configurations. In order to achieve higher flight speed in the rotor failure conditions, the weight of the drone is reduced by lightening the battery. The incremental nonlinear dynamic inversion (INDI) method has been applied to control the drone in SRF case in the wind tunnel. Details about the method can be found in [16]. The controller of a quadrotor in the DRF configuration will be introduced in an upcoming report.

In the SRF and DRF configuration, the drone fast spins on the yaw direction at about 20 rad/s. By making use of this effect, the in-plane force of the rotor can be easily extracted from the damping on the yaw direction. In these two configurations, the drone is able to reach up to 9 m/s flight speed. The measured inertial and geometric properties of the tested quadrotor in different falure conditions are listed in Table I.

IV. Data Preprocessing

A. Force and Moment Measurement

The specific force acting on the IMU, denoted by $\boldsymbol{a}^B$, can be obtained from the unbiased accelerometer measurement after the ground calibrations. However, for the high-rate spinning quadrotor, a horizontal supporting force is acting on the accelerometer to compensate for the centrifugal force caused by the displacement between the c.g. and the IMU location. Roughly speaking, this centrifugal force can reach about 1 m/s^2 with displacement less than 3 mm.

Although this displacement, denoted by $\boldsymbol{d}^B_{ca}$, can be inconsistent in different flights and too minute to measure, it can be estimated from the flight data. According to [18], the real external force acting on the c.g. is

$$\frac{1}{m}\begin{bmatrix} F_x \\ F_y \end{bmatrix} = \begin{bmatrix} a_x \\ a_y \end{bmatrix} - \begin{bmatrix} -(q^2+r^2) & pq-\dot{r} & pr+\dot{q} \\ pq+\dot{r} & -(r^2+p^2) & qr-\dot{p} \end{bmatrix} \boldsymbol{d}^B_{ca} \tag{10}$$

An approximation is made that the external horizontal force is zero during the relaxed hovering flight [19]:

$$F_x = F_y = 0$$

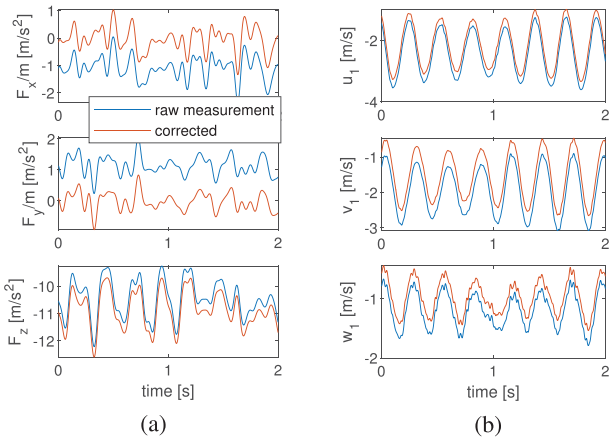

(a) (b)

Fig. 4. (a) Comparison between the accelerometer measured external force before and after the correctness considering $\boldsymbol{d}_{ca}^{B}$, where $\hat{\boldsymbol{d}}_{ca}^{B} = [1.8,\ -2.7,\ 0.4]^{T}$mm. (b) The local air-velocity estimation of a rotor before and after correction considering $\boldsymbol{d}_{oa}^{B}$, where $\hat{\boldsymbol{d}}_{oa}^{B} = [23.4,\ 1.5,\ 23.8]^{T}$mm.

Then $\boldsymbol{d}_{ca}^{B}$ can be estimated by a Least Square estimator using (10). After knowing the estimation $\hat{\boldsymbol{d}}_{ca}^{B}$, we can in turn obtain the measurement of $\boldsymbol{F}^{B}$ on c.g. as follows

$$\frac{1}{m}\boldsymbol{F}_{\text{mea}}^{B} = \boldsymbol{a}^{B} - \frac{d\boldsymbol{\Omega}^{B}}{dt} \times \hat{\boldsymbol{d}}_{ca}^{B} - \boldsymbol{\Omega}^{B} \times \left(\boldsymbol{\Omega}^{B} \times \hat{\boldsymbol{d}}_{ca}^{B}\right) \quad (11)$$

The original measured specific force and the corrected specific force are compared as shown in Fig. 4a.

The moment measurement $\boldsymbol{M}_{\text{mea}}^{B}$ can be obtained using (2), with the knowledge of inertial properties given in Table I. It is worth noting that, for SRF/DRF configurations, the gyroscopic moments from rotors cannot be neutralized by counter-rotating propellers due to the loss of rotors. Therefore, $\boldsymbol{I}_{p}^{B}$ is estimated by making a CAD model to ensure the accuracy of the estimation of the gyroscopic moment. The accelerometer measured $\boldsymbol{a}^{B}$, the gyroscopic measured $\boldsymbol{\Omega}^{B}$ and the BLDC measured ω_i are bi-directionally filtered by a 4th order Butterworth filter with 15 Hz cut-off frequency.

B. Velocity Reconstruction

The air velocity of c.g., namely $\boldsymbol{V}^{B}$, and the local air velocity each rotor $\boldsymbol{V}_{i}^{B}$ should be characterized as independent variables of the proposed model. However, the slight displacement from the motion capturing system measured reference point to the IMU location could bring nonnegligible effects on these air-velocities due to the spinning motion in the SRF/DRF configurations.

The velocity of c.g. with respect to the airflow can be measured indirectly by

$$\boldsymbol{V}^{B} = \boldsymbol{\Omega}^{B} \times \left(\boldsymbol{d}_{oa}^{B} - \boldsymbol{d}_{ca}^{B}\right) + \boldsymbol{L}_{BI}\left(\boldsymbol{V}_{o}^{I} - \boldsymbol{V}_{w}^{I}\right) \quad (12)$$

where $\boldsymbol{V}_{o}^{I}$ is the velocity measured by the OptiTrack; $\boldsymbol{d}_{oa}^{B}$ is the displacement from the OptiTrack measured point to the IMU location. $\boldsymbol{d}_{ca}^{B}$ is the displacement from IMU location to c.g., which can be estimated using the method given in Sec. IV-A.

Similarly, the local air-velocity of the ith rotor can be measured indirectly by

$$\boldsymbol{V}_{i}^{B} = \boldsymbol{\Omega}^{B} \times (\boldsymbol{d}_{oa}^{B} + \boldsymbol{d}_{ai}^{B}) + \boldsymbol{L}_{BI}(\boldsymbol{V}_{o}^{I} - \boldsymbol{V}_{w}^{I}) \quad (13)$$

where $\boldsymbol{d}_{ai}^{B}$ represents the displacement from the IMU to the center of the ith rotor, which is consistent and can be measured accurately.

From the practical standpoint, $\boldsymbol{d}_{oa}^{B}$ in (12) and (13) can be variable in different experiments. Here we introduce a method to determine $\boldsymbol{d}_{oa}^{B}$ using the flight data. The velocity of IMU with respect to the inertial frame can be expressed as

$$\boldsymbol{V}_{a}^{B} = \boldsymbol{L}_{BI}\boldsymbol{V}_{o}^{I} + \boldsymbol{\Omega}^{B} \times \boldsymbol{d}_{oa}^{B} \quad (14)$$

By taking derivative of both sides of the above equation and projecting on the body frame, we have

$$\boldsymbol{a}^{B} + \boldsymbol{L}_{BI}\left(\boldsymbol{g}^{I} - \dot{\boldsymbol{V}}_{o}^{I}\right) = \left(\dot{\boldsymbol{\Omega}}_{\times}^{B} + \boldsymbol{\Omega}_{\times}^{B}\boldsymbol{\Omega}_{\times}^{B}\right)\boldsymbol{d}_{oa}^{B} \quad (15)$$

where $\boldsymbol{\Omega}_{\times}$ denotes the skew-symmetric matrix such that $\boldsymbol{\Omega}_{\times}\boldsymbol{v} = \boldsymbol{\Omega} \times \boldsymbol{v}$ for any $\boldsymbol{v} \in \mathbb{R}^{3}$. We hereby use $\hat{\boldsymbol{L}_{BI}}$ to represents the estimated rotational matrix from the EKF. Then the estimation of $\boldsymbol{d}_{oa}^{B}$, denoted by $\hat{\boldsymbol{d}}_{oa}^{B}$, can be obtained by

$$\hat{\boldsymbol{d}}_{oa}^{B} = \left(\dot{\boldsymbol{\Omega}}_{\times}^{B} + \boldsymbol{\Omega}_{\times}^{B}\boldsymbol{\Omega}_{\times}^{B}\right)^{-1}\left[\boldsymbol{a}^{B} + \hat{\boldsymbol{L}_{BI}}\left(\boldsymbol{g}^{I} - \dot{\boldsymbol{V}}_{o}^{I}\right)\right] \quad (16)$$

Subsequently, the air-velocities can be obtained from (12) and (13). For demonstration, the local air-velocity of the 1st rotor during a set of flight with SRF configuration are plotted in Fig. 4(b). It shows that the horizontal velocity estimation is quite different after considering the effect of $\boldsymbol{d}_{oa}^{B}$, because the yaw rate is over 20 rad/s during this flight.

The estimated rotational matrix $\hat{\boldsymbol{L}_{BI}}$, however, can be deviated from the real value due to the orientation difference between the OptiTrack measurements and the body frame. We hereby define the estimation error as $\Delta\boldsymbol{L}_{BI}$ for quantification, such that

$$\boldsymbol{L}_{BI} = (\boldsymbol{I}_{3\times3} - \Delta\boldsymbol{L}_{BI})\hat{\boldsymbol{L}_{BI}} \quad (17)$$

By substituting (16) and (17) into (15), we have

$$\left(\dot{\boldsymbol{\Omega}}_{\times}^{B} + \boldsymbol{\Omega}_{\times}^{B}\boldsymbol{\Omega}_{\times}^{B}\right)\Delta\boldsymbol{d}_{oa}^{B} = \Delta\boldsymbol{L}_{BI}\hat{\boldsymbol{L}_{BI}}\left(\boldsymbol{g}^{I} - \frac{d\boldsymbol{V}_{o}^{I}}{dt}\right) \quad (18)$$

where $\Delta\boldsymbol{d}_{oa}^{B} = \hat{\boldsymbol{d}}_{oa}^{B} - \boldsymbol{d}_{oa}^{B}$ is the estimation error of $\boldsymbol{d}_{oa}^{B}$. By substituting $\Delta\boldsymbol{d}_{oa}^{B}$ and (17) into (12) and (13), we can derive the estimation error of velocities due to the error of the attitude estimation:

$$\Delta\boldsymbol{V}^{B} = \Delta\boldsymbol{V}_{i}^{B} = \boldsymbol{\Omega}_{\times}^{B}\Delta\boldsymbol{d}_{oa}^{B} + \Delta\boldsymbol{L}_{BI}\hat{\boldsymbol{L}_{BI}}\left(\boldsymbol{V}_{o}^{I} - \boldsymbol{V}_{w}^{I}\right) \quad (19)$$

Fig. 5 demonstrates the average relative error of velocity $E[|\Delta\boldsymbol{V}|/|\boldsymbol{V}|]$ versus the L^{2} norm of $\Delta\boldsymbol{L}_{BI}$ using (19) where the other variables in (19) are from a set of flight data. It is clear that the velocity estimation error grows with the increase of $|\Delta\boldsymbol{L}_{BI}|$. If we set the maximum velocity relative error as 5%, for example, $|\Delta\boldsymbol{L}_{BI}|$ need to be smaller than 0.22, which is easy to fulfil for most attitude estimators.

V. Model Identification

In this section, the aerodynamic model is identified from the preprocessed data. A parametric model is established with

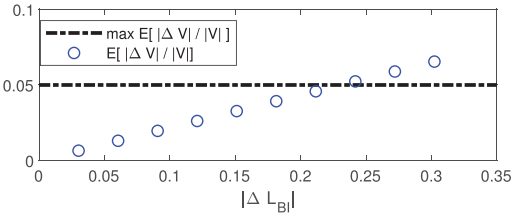

Fig. 5. Average relative error of velocity ($E[|\Delta \boldsymbol{V}|/|\boldsymbol{V}|]$) versus the attitude estimation error represented by $|\Delta \boldsymbol{L}_{BI}|$. The velocity error grows with the increase of $|\Delta \boldsymbol{L}_{BI}|$.

model structures predefined in the form of polynomials based on physical insight. Compared with the non-parametric model, the parametric model is less tend to overfit and requires less computational effort. By virtue of these advantages, it has been widely used in the aircraft model identification applications (see, e.g., [18]).

First of all, a simplified model structure of the in-plane forces and the pitch/roll moments of a single is derived. Most of the multi-rotor vehicles employ fixed-pitch rotors with elasticity. Due to the imbalanced lift between the advancing and retreating blades with the existence of airspeed, the tip-path-plane tilts backward and sideways with respect to the air stream. This brings several consequences. First of all, the thrust has a projection on the rotor plane and contributes to the in-plane force [8]. Secondly, due to the resilience of the rotor blade, the pitch and roll moments are generated with respect to the rotor hub [6], [9]. The latter is usually omitted because of the symmetric property of the quadrotor. However, these moments have to be taken in to account with the occurrence of rotor failures.

The identified model is usually valid within the test regime covering the flight data. To improve the validity of the model for extrapolation, the structure should be chosen as simple as possible while capturing the major effects.

For the ith rotor, define a 2-D vector named horizontal advance ratio and its perpendicular vector as

$$\boldsymbol{\mu}_i = [u_i,\ v_i]^T/\omega_i R,\quad \boldsymbol{\mu}_i^{\perp} = [-v_i,\ u_i]^T/\omega_i R \tag{20}$$

Usually $\frac{1}{2}|\boldsymbol{\mu}_i|^2 \ll 1$, then a simple model of the rotor flapping angle can be expressed as [8]

$$\begin{aligned}\boldsymbol{\beta} &= -\boldsymbol{\mu}_i A_{1,c}/\left(1-\tfrac{1}{2}|\boldsymbol{\mu}_i|^2\right) \approx -\boldsymbol{\mu}_i A_{1,c}\\ \boldsymbol{\beta}^{\perp} &= -\boldsymbol{\mu}_i^{\perp} s_{n,i} A_{1,s}/\left(1-\tfrac{1}{2}|\boldsymbol{\mu}_i^{\perp}|^2\right) \approx -\boldsymbol{\mu}_i^{\perp} s_{n,i} A_{1,s}\end{aligned} \tag{21}$$

where $A_{1,c}$ and $A_{1,s}$ are constants. Vectors $\boldsymbol{\beta}$ and $\boldsymbol{\beta}^{\perp}$ contain the information about flapping angles along and perpendicular to the incoming flow. The norms of both vectors indicate the magnitude of the flapping angle as the elements indicate the flapping direction expressed in the $x_B - y_B$ plane.

By assuming that the flapping angles are small and using (6), the in-plane forces of the ith rotor due to the blade-flapping effect can be approximated by

$$\begin{bmatrix}F_{x,i}\\ F_{y,i}\end{bmatrix} \approx T_i(\boldsymbol{\beta}+\boldsymbol{\beta}^{\perp}) = C_{t,i}\pi R^3 \rho \omega_i \begin{bmatrix}-A_{1,c}u_i + A_{1,s}s_{n,i}v_i\\ -A_{1,c}v_i - A_{1,s}s_{n,i}u_i\end{bmatrix} \tag{22}$$

We assume a constant $C_{t,i}$ for simplicity of the model, then (22) can be re-written as

$$\begin{bmatrix}F_{x,i}\\ F_{y,i}\end{bmatrix} = k_1 \begin{bmatrix}u_i\omega_i\\ v_i\omega_i\end{bmatrix} + k_2 \begin{bmatrix}v_i s_{n,i}\omega_i\\ -u_i s_{n,i}\omega_i\end{bmatrix} \tag{23}$$

where k_1 and k_2 are parameters to be identified.

The roll/pitch moment of a single rotor can be caused by two major effects: The elastic moment due to the blade flapping [6], and the in-plane force generated moment with respect to the c.g.. Therefore, we assume that the moment aligns with the rotor plan tilted direction and a simplified model structure is selected as

$$\begin{bmatrix}M_{x,i}\\ M_{y,i}\end{bmatrix} = k_3 \begin{bmatrix}-v_i\omega_i\\ u_i\omega_i\end{bmatrix} + k_4 \begin{bmatrix}u_i s_{n,i}\omega_i\\ v_i s_{n,i}\omega_i\end{bmatrix} \tag{24}$$

In the high-speed flight, the forces and moments from the airframe become apparent and are modeled as

$$\boldsymbol{F}_f = \frac{1}{2}\rho|\boldsymbol{V}|^2 S[C_x,\ C_y,\ C_z]^T \tag{25}$$

$$\boldsymbol{M}_f = \frac{1}{2}\rho|\boldsymbol{V}|^2 Sb[C_l,\ C_m,\ C_n]^T \tag{26}$$

where $S = 4lb$ is defined as the reference area; C_x to C_n are modeled as functions of air-velocity of the c.g.. These coefficients need to capture most of the aerodynamic effects on the airframe. Therefore, the model structure of these coefficients are selected as follows. First of all, define the normalized velocities as

$$[\bar{u},\ \bar{v},\ \bar{w}]^T = \frac{[u,\ v,\ w]^T}{\sqrt{u^2+v^2+w^2}} = \left[\frac{u}{|\boldsymbol{V}|},\ \frac{v}{|\boldsymbol{V}|}\ \ \frac{w}{|\boldsymbol{V}|}\right]^T \tag{27}$$

To prevent singularity, define

$$[\bar{u},\ \bar{v},\ \bar{w}]^T = [0,\ 0,\ 0]^T,\quad \text{when } |\boldsymbol{V}| = 0 \tag{28}$$

Noting that $\bar{w}$ can be analogous to the angle of attack while $\bar{v}$ is analogous to the side-slip angle of a fixed-wing aircraft. Normalizing the velocity could prevent extrapolation of the model and increase its stability.

Then the model structures of these aerodynamic coefficients are selected as follows

$$\begin{aligned}\begin{bmatrix}C_x\\ C_y\\ C_z\\ C_l\\ C_m\\ C_n\end{bmatrix} &= \begin{bmatrix}\operatorname{sgn}(\bar{u})\left[|\bar{u}|,\ \bar{u}^2\right]\boldsymbol{K_x}\\ \operatorname{sgn}(\bar{v})\left[|\bar{v}|,\ \bar{v}^2\right]\boldsymbol{K_y}\\ \operatorname{sgn}(\bar{w})\left[|\bar{w}|,\bar{w}^2\right]\\ \operatorname{sgn}(\bar{v})[|\bar{v}|,\ \bar{v}^2,\ |\bar{v}|\bar{w},\ |\bar{v}|^3,\ \bar{v}^2\bar{w},\ |\bar{v}|\bar{w}^2]\boldsymbol{K_l}/b\\ \operatorname{sgn}(\bar{u})[|\bar{u}|,\ \bar{u}^2,\ |\bar{u}|\bar{w},\ |\bar{u}|^3,\ \bar{u}^2\bar{w},\ |\bar{u}|\bar{w}^2]\boldsymbol{K_m}/b\\ \operatorname{sgn}(\bar{u})\operatorname{sgn}(\bar{v})[|\bar{v}|,\ \bar{v}^2,\ |\bar{v}|\bar{u},\ |\bar{v}|^3,\ \bar{v}^2\bar{u},\ |\bar{v}|\bar{u}^2]\boldsymbol{K_n}/b\end{bmatrix}\\ &= \mathbf{P}\left[\boldsymbol{K_x}^T,\ \boldsymbol{K_y}^T,\ \boldsymbol{K_z}^T,\ \boldsymbol{K_l}^T,\ \boldsymbol{K_m}^T,\ \boldsymbol{K_n}^T\right]^T\end{aligned} \tag{29}$$

where $\boldsymbol{K_x}$ to $\boldsymbol{K_n}$ are arrays of parameters to identify. This model structure is selected to capture the major aerodynamic effects while minimizing the number of terms in the model to facilitate estimation. For instance, the C_x is found to be mostly affected by u and should be zero while the drone is conducting vertical ($\bar{w} = \pm 1,\ \bar{u} = \bar{v} = 0$) and sidewards ($\bar{v} = \pm 1,\ \bar{u} = \bar{w} = 0$) maneuvers. Therefore, C_x model is selected as a second order polynomial of $\bar{u}$. Similarly, C_m is known to be affected by the angle of attack and side-slip angle [20]. Then we use $\bar{w}$ and $\bar{u}$ to capture the effect of these angles, and at the same time,

guarantee that the pitch moment should be zero while doing vertical and sideways maneuvers. To cope with the symmetry of the drone, the absolute value of $\bar{u}$ and the sign function $\mathrm{sgn}(\cdot)$ are implemented. The model structure information is then summarized in the matrix $\mathbf{P}$ in (29).

Consequently, substituting (23)–(26) and (29) into (4) yields a model that is linear in parameters

$$\boldsymbol{Y} = \boldsymbol{A}\boldsymbol{K} + \boldsymbol{\epsilon} \tag{30}$$

where $\boldsymbol{\epsilon}$ is the model residual, and $\boldsymbol{A}$, $\boldsymbol{K}$ and $\boldsymbol{Y}$ are given in (31) shown at the bottom of this page. Note that T_i and $M_{z,i}$ in $\boldsymbol{Y}$ are not measured but calculated from the static test obtained model using (6) and (7).

With N measurement samples, the regressor matrix $\mathbf{A}$ and the total output $\boldsymbol{Z}$ are defined as

$$\boldsymbol{G} = \left[\boldsymbol{A}_1^T, \ldots, \boldsymbol{A}_N^T\right]^T, \quad \boldsymbol{Z} = \left[\boldsymbol{Y}_1^T, \ldots, \boldsymbol{Y}_N^T\right]^T \tag{32}$$

Since the forces and moments have different orders of magnitude, a weight least square (WLS) estimator is applied:

$$\boldsymbol{K} = (\boldsymbol{G}^T\boldsymbol{W}\boldsymbol{G})^{-1}\boldsymbol{G}^T\boldsymbol{W}\boldsymbol{Z} \tag{33}$$

The weighting matrix is select to be

$$\boldsymbol{W} = \mathrm{diag}(\overbrace{1,1,1,200,200,200,\ldots,1,1,1,200,200,200}^{N\times 6}) \tag{34}$$

which indicates that the moments measurements have larger weighting because of their smaller magnitude compared to the forces.

The key parameters in the model are listed in Appendix. Based on (23) and (24), apart from the in-plane force along the coming flow, there exists a force that is right side perpendicular to the coming flow. A pitch up moment and a roll moment to the left are also generated. Fig. 6 presents the aerodynamic coefficients of the airframe. The force related coefficients are negatively related to the normalized speeds, which is in line with the physics view. In addition, the moment models present aerodynamic instabilities of the airframe. For instance, the pitch up moment grows with the increase of angle of attack.

VI. Model Validation

Several sets of flight data in SRF and norminal configurations are compared with the preceding model to show its validity.

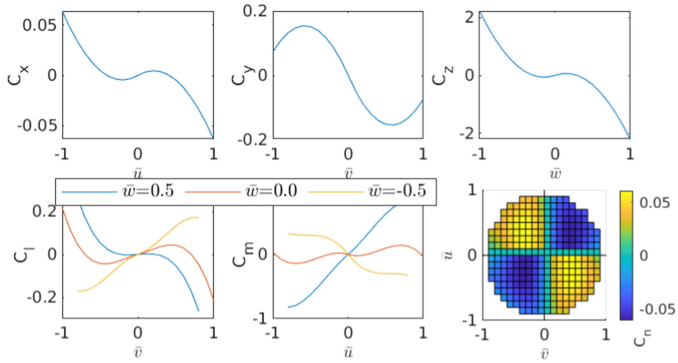

Fig. 6. The aerodynamic coefficients model of the airframe identified from the flight data.

Note that these data are independent from those used for model estimation. For comparison, a commonly used lumped parameters model ([7], [19]), in combine with the T_i and $M_{z,i}$ model obtained during the static wind tunnel test of this research, is introduced as the benchmark

$$\begin{aligned} F_x &= c_1 u + c_2 u^2, \quad F_y = c_3 v + c_4 v^2, \quad F_z = -\sum T_i, \\ M_x &= \sum b s_{l,i} T_i + c_5 p^2, \quad M_y = \sum l s_{m,i} T_i + c_6 q^2, \\ M_z &= \sum M_{z,i} + c_7 r^2 \end{aligned} \tag{35}$$

where c_1–c_7 are constants, T_i and $M_{z,i}$ are obtained from (6) and (7) using the rotor C_t and C_q data obtained from the static wind tunnel test.

Case 1: One set of flight data with SRF configuration is used for validating the aerodynamic forces/moments. In this flight, the left-back rotor (rotor 4) is removed and the drone spins at the yaw rate $r \approx -20$ rad/s. Fig. 7 presents the aerodynamic predictions using two models, together with their normalized root mean square error (NRMS). Both models perform well at $V = 2$ m/s whereas the proposed model performs better at $V = 8$ m/s when aerodynamic effects become apparent.

Case 2: Define the lateral force perpendicular to the free stream as

$$F_{\text{lateral}} = [0,\ 1,\ 0]\boldsymbol{L}_{IB}[F_x,\ F_y, 0]^T \tag{36}$$

Noting that $F_{\text{lateral}} = 0$ for NF case with zero side-slip. However, as was observed in a previous research [16], this lateral

$$\boldsymbol{A} = \left[\begin{array}{cccc:c} \sum u_i\omega_i & \sum v_i s_{n,i}\omega_i & 0 & 0 & \\ \sum v_i\omega_i & -\sum u_i s_{n,i}\omega_i & 0 & 0 & \\ 0 & 0 & 0 & 0 & \\ 0 & 0 & -\sum v_i\omega_i & \sum s_{n,i}u_i\omega_i & \frac{1}{2}\rho|\boldsymbol{V}|^2 S\,\mathbf{P} \\ 0 & 0 & \sum u_i\omega_i & \sum s_{n,i}v_i\omega_i & \\ \sum (b s_{l,i}u_i + l s_{m,i}v_i)\omega_i & \sum (b s_{l,i}v_i - l s_{m,i}u_i)s_{n,i}\omega_i & 0 & 0 & \end{array}\right],$$

$$\boldsymbol{Y} = \left[F_x,\ F_y,\ F_z + \sum T_i,\ M_x - \sum s_{l,i} b T_i,\ M_y - \sum s_{n,i} l T_i,\ M_z - \sum M_{z,i}\right]^T,$$

$$\boldsymbol{K} = \left[k_1,\ k_2,\ k_3,\ k_4,\ \boldsymbol{K_x}^T,\ \boldsymbol{K_y}^T,\ \boldsymbol{K_z}^T,\ \boldsymbol{K_l}^T,\ \boldsymbol{K_m}^T,\ \boldsymbol{K_n}^T\right]^T \tag{31}$$

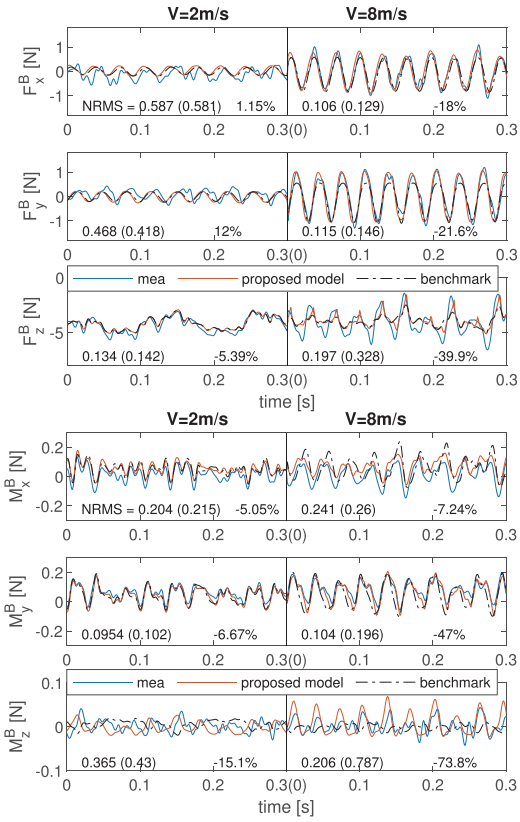

Fig. 7. Validation result of $\boldsymbol{F}^B$ and $\boldsymbol{M}^B$ with the SRF configuration at the airspeed of 2 m/s and 8 m/s. The normalized RMS (NRMS) is given for both the proposed model and the benchmark model (in parentheses), together with the percentage change of the NRMS.

force is non-zero for the spinning quadrotor with single rotor failure.

The direction of this lateral force is also correlated to the yaw rate direction. Specifically, a positive yaw rate ($r > 0$) leads to a lateral force towards the right with respect to the flight direction; a negative yaw rate could lead to a force to the left. This is probably due to the speed up of the rotor behind the airframe with respect to the air stream that brings larger in-plane force than the other rotors. Fig. 8 compares the measured F_{lateral} and both the proposed model and the benchmark, together with trend lines illuminating the model performance. It is obvious that the proposed model can well predict this effect, while the lateral force can be hardly captured by the benchmark model.

Case 3: Apart from the cases with rotor failures, the model also needs to be effective for the quadrotor in the no-failure configuration. This is validated by calculating the longitudinal trim curve using the models and comparing with the measurement. The longitudinal trim curve of a quadrotor was defined in [21] as the rotor speeds and the pitch angle during the level flight at different airspeed. The trim curve reveals that the rear rotors should rotate faster than front rotors during the forward flight. As Fig. 9 shows, the proposed model can capture this effect and fit the measured data in the whole range of airspeed, despite slight mismatch at 2–8 m/s. In comparison, this distinction cannot be captured by the benchmark model, and the data fitting is unsatisfactory.

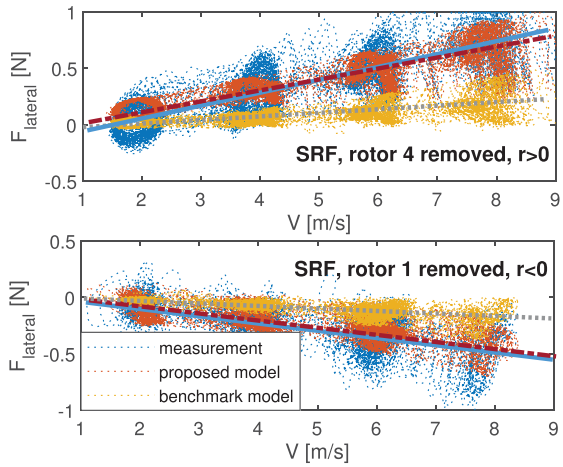

Fig. 8. Aerodynamic force perpendicular to the air velocity (considered positive to the right with respect to the air velocity). Comparison among the measurement (blue), the proposed model (red) and the benchmark model (yellow), of which trend lines are given in blue-solid, red-dash-dot and gray-dot respectively.

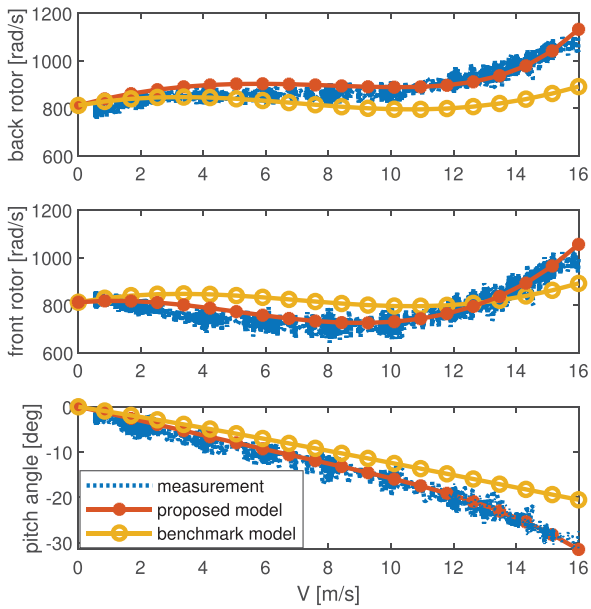

Fig. 9. Rotor speeds and pitch angle during the level forward flight at different flight speeds with the nominal configuration. Comparison between the model prediction and the flight data.

VII. Conclusions

In this research, the aerodynamic force/moment model of a quadrotor has been identified in the high-speed flight regime. A multi-body parametric model is selected to balance between accuracy and simplicity, and the model is versatile to fit different flight conditions. To cope with fast spinning motion in rotor failure configurations, a novel correction method for specific force and velocity measurements has been developed considering the location mismatch among IMU, c.g. and the reference point of the motion capturing system.

The proposed model has been validated in both nominal cases and with rotor failures. The comparison also shows advantages

with respect to the lumped parameters benchmark model, particularly in the high-speed flight regime. Other complex effects such as the vortex-ring effect, ceiling/ground effect may be modeled in future research.

APPENDIX

The parameters of the proposed model for a Bebop2 quadrotor are given as follows. Readers may access the model in MATLAB script via https://bitbucket.org/SihaoSun/bebop2_aerodynamic_model. The model is valid when the airspeed $V \in [0,\ 16]$ m/s. Model beyond this range may have deficient accuracy.

$$[k_1,\ k_2,\ k_3,\ k_4] = [-3.96,\ 2.29,\ 0.464, -0.0966] \times 10^{-5}$$

$$\boldsymbol{K_x} = [3.00, -8.92]^T \times 10^{-2}$$
$$\boldsymbol{K_y} = [-0.509,\ 0.400]^T$$
$$\boldsymbol{K_z} = [0.838, -2.85]^T$$
$$\boldsymbol{K_l} = [1.17, -0.0498,\ 1.69, -2.65,\ 6.24, -4.57]^T \times 10^{-2}$$
$$\boldsymbol{K_m} = [-8.46,\ 27.6,\ 10.2, -19.4,\ 3.62,\ 1.98]^T \times 10^{-2}$$
$$\boldsymbol{K_n} = [-3.07,\ 7.59, -1.34, -4.51,\ 1.55, -0.572]^T \times 10^{-2}$$

$$\begin{aligned}\boldsymbol{K}_{Ct} = [\ & 0.0156,\ -0.0552,\ 0.684,\ -2.24,\ 3.05, -1.52,\\ & -0.0145,\ 0.457,\ -0.525,\ 0.233,\ -0.0258,\ 0.0401,\\ & -0.0116,\ -0.00223,\ -0.0225,\ 0.00336]^T\end{aligned}$$

$$\begin{aligned}\boldsymbol{K}_{Cq} = [\ & -0.00227, -0.00113,\ 0.00368, -0.101,\ 0.226,\\ & -0.146, -0.00305, -0.00748, -0.111,\\ & 0.121, 0.00336, 0.00363, -0.00729,\\ & 0.00116,\ 0.00257, -0.000681]^T\end{aligned}$$

ACKNOWLEDGMENT

The authors would like to thank K. Kersbergen, MAVLab, and High Speed Lab of Delft University of Technology for their assistance during the tests.

REFERENCES

[1] S. Waslander and C. Wang, "Wind disturbance estimation and rejection for quadrotor position control," in *Proc. AIAA Infotech@Aerospace Conf.*, Reston, VA, USA, Apr. 2009, pp. 1935–1948.

[2] S. Kim, D. Falanga, and D. Scaramuzza, "Computing the forward reachable set for a multirotor under first-order aerodynamic effects," *IEEE Robot. Autom. Lett.*, vol. 3, no. 4, pp. 2934–2941, Oct. 2018.

[3] T. Carroll, I.-R. E. George, and G. Bramesfeld, "Design optimization of small rotors in quad-rotor configuration," in *Proc. 54th AIAA Aerosp. Sci. Meeting*, Jan. 2016, pp. 1–17.

[4] H. Huang, G. Hoffmann, S. Waslander, and C. Tomlin, "Aerodynamics and control of autonomous quadrotor helicopters in aggressive maneuvering," in *Proc. IEEE Int. Conf. Robot. Autom.*, May 2009, pp. 3277–3282.

[5] G. Hoffmann, H. Huang, S. Waslander, and C. Tomlin, "Quadrotor helicopter flight dynamics and control: Theory and Experiment," in *Proc. AIAA Guid., Navigat., Control Conf. Exhibit*, Aug. 2007, vol. 4, pp. 1–20.

[6] G. M. Hoffmann, H. Huang, S. L. Waslander, and C. J. Tomlin, "Precision flight control for a multi-vehicle quadrotor helicopter testbed," *Control Eng. Pract.*, vol. 19, pp. 1023–1036, Sep. 2011.

[7] M. Schulz, F. Augugliaro, R. Ritz, and R. D'Andrea, "High-speed, steady flight with a quadrocopter in a confined environment using a tether," in *Proc. IEEE/RSJ Int. Conf. Intell. Robots Syst.*, Sep. 2015, pp. 1279–1284.

[8] R. Mahony, V. Kumar, and P. Corke, "Multirotor aerial vehicles: modeling, estimation, and control of quadrotor," *IEEE Robot. Autom. Mag.*, vol. 19, no. 3, pp. 20–32, Sep. 2012.

[9] P. Bristeau, P. Martin, E. Salaun, and N. Petit, "The role of propeller aerodynamics in the model of a quadrotor UAV," in *Proc. Eur. Control Conf.*, Aug. 2009, pp. 683–688.

[10] C. Russell, J. Jung, G. Willink, and B. Glasner, "Wind tunnel and hover performance test results for multicopter UAS vehicles," in *Proc. AHS Annu. Forum*, 2016, pp. 1–20.

[11] S. Sun, C. C. de Visser, and Q. Chu, "Quadrotor gray-box model identification from high-speed flight data," *J. Aircr.*, vol. 56, no. 2, pp. 645–661, Mar. 2019.

[12] M. Burri, J. Nikolic, H. Oleynikova, M. W. Achtelik, and R. Siegwart, "Maximum likelihood parameter identification for MAVs," in *Proc. IEEE Int. Conf. Robot. Autom.*, 2016, pp. 4297–4303.

[13] J. Svacha, K. Mohta, and V. Kumar, "Improving quadrotor trajectory tracking by compensating for aerodynamic effects," in *Proc. Int. Conf. Unmanned Aircr. Syst.*, Jun. 2017, pp. 860–866.

[14] J. M. Kai, G. Allibert, M. D. Hua, and T. Hamel, "Nonlinear feedback control of quadrotors exploiting first-order drag effects," *IFAC-PapersOnLine*, vol. 50, no. 1, pp. 8189–8195, 2017.

[15] D. Kaya and A. T. Kutay, "Aerodynamic modeling and parameter estimation of a quadrotor helicopter," in *Proc. AIAA Atmos. Flight Mech. Conf.*, Jun. 2014, pp. 1–28.

[16] S. Sun, L. Sijbers, X. Wang, and C. de Visser, "High-speed flight of quadrotor despite loss of single rotor," *IEEE Robot. Autom. Lett.*, vol. 3, no. 4, pp. 3201–3207, Oct. 2018.

[17] "TDK invensense MPU-6050." Accessed: Feb. 20, 2019. [Online]. Available: https://www.invensense.com/products/motion-tracking/6-axis/mpu-6050/

[18] V. Klein and E. A. Morelli, *Aircraft System Identification: Theory and Practice*. Reston, VA, USA: Amer. Inst. Aeronaut. Astronaut., Jan. 2006.

[19] M. W. Mueller and R. D'Andrea, "Relaxed hover solutions for multicopters: Application to algorithmic redundancy and novel vehicles," *Int. J. Robot. Res.*, vol. 35, pp. 873–889, Jul. 2016.

[20] J. V. Foster and D. Hartman, "High-fidelity multi-rotor unmanned aircraft system (UAS) simulation development for trajectory prediction under off-nominal flight dynamics," in *Proc. 17th AIAA Aviation Technol., Integr., Oper. Conf.*, Jun. 2017, pp. 1–19.

[21] S. Sun and C. C. de Visser, "Quadrotor safe flight envelope prediction in the high-speed regime: A Monte-Carlo approach," in *Proc. AIAA Scitech 2019 Forum*, Jan. 2019, pp. 1–12.